Title

Predicting the effects of dATP on cardiac contraction using multiscale modeling of the sarcomere

Authors

McCabe, Kimberly J

Aboelkassem, Yasser

Teitgen, Abigail E

et al.

Publication Date

2020-11-01

DOI

10.1016/j.abb.2020.108582

Peer reviewed

Published in final edited form as:

Arch Biochem Biophys. 2020 November 30; 695: 108582. doi:10.1016/j.abb.2020.108582.

Predicting the effects of dATP on cardiac contraction using multiscale modeling of the sarcomere

Kimberly J. McCabe[a], **Yasser Aboelkassem**[b], **Abigail E. Teitgen**[c], **Gary A. Huber**[d], **J. Andrew McCammon**[d], **Michael Regnier**[e], **Andrew D. McCulloch**[c]

[a]Simula Research Laboratory, Department of Computational Physiology, PO Box 134, 1325 Lysaker, Norway

[b]San Diego State University, Department of Mechanical Engineering, 5500 Campanile Drive San Diego, CA 92182

[c]University of California San Diego, Department of Bioengineering, 9500 Gilman Drive MC 0412 La Jolla, CA 92093

[d]University of California San Diego, Department of Chemistry & Biochemistry, 9500 Gilman Drive, MC 0303 La Jolla, CA 92093

[e]University of Washington, Department of Bioengineering, Box 355061 Seattle, WA 98195

Abstract

2'-deoxy-ATP (dATP) is a naturally occurring small molecule that has shown promise as a therapeutic because it significantly increases cardiac myocyte force development even at low dATP/ATP ratios. To investigate mechanisms by which dATP alters myosin crossbridge dynamics, we used Brownian dynamics simulations to calculate association rates between actin and ADP- or dADP-bound myosin. These rates were then directly incorporated in a mechanistic Monte Carlo Markov Chain model of cooperative sarcomere contraction. A unique combination of increased powerstroke and detachment rates was required to match experimental steady-state and kinetic data for dATP force production in rat cardiac myocytes when the myosin attachment rate in the model was constrained by the results of a Brownian dynamics simulation. Nearest-neighbor cooperativity was seen to contribute to, but not fully explain, the steep relationship between dATP/ATP ratio and steady-state force-development observed at lower dATP concentrations. Dynamic twitch simulations performed using measured calcium transients as inputs showed that

Corresponding Author: Kimberly J. McCabe, kimberly@simula.no.

K.J.M: Conceptualization, Methodology, Software, Writing - Original Draft, Visualization, Investigation. **Y.A.**: Software, Data Curation. **A.E.T.**: Investigation, Validation. **G.A.H**: Software, Writing- Reviewing and Editing. **J.A.M.**: Supervision, Writing-Reviewing and Editing, Funding acquisition, Resources. **M.R.:** Supervision, Conceptualization, Funding acquisition. **A.D.M:** Supervision, Conceptualization, Funding acquisition, Writing- Reviewing and Editing, Resources.

[6]Declarations of interest

A. D. McCulloch is a co-founder of and has an equity interest in Insilicomed and Vektor Medical. He serves on the scientific advisory board of Insilicomed and as scientific advisor to both companies. Some of his research grants, including those acknowledged here, have been identified for conflict of interest management based on the overall scope of the project and its potential benefit to these companies.

the effects of dATP on the crossbridge alone were not sufficient to explain experimentally observed enhancement of relaxation kinetics by dATP treatment. Hence, dATP may also affect calcium handling even at low concentrations. By enabling the effects of dATP on sarcomere mechanics to be predicted, this multi-scale modelling framework may elucidate the molecular mechanisms by which dATP can have therapeutic effects on cardiac contractile dysfunction.

Keywords

multiscale modeling; sarcomere; brownian dynamics; myosin; cardiac contractility

1 Introduction

2'-deoxy-ATP (dATP) is a small molecule which is present in most cell types due to its primary role as a building block of DNA. When dATP replaces ATP in cardiomyocytes, it has been shown to increase force production, enhance crossbridge cycling speed, and accelerate the removal of Ca^{2+} from the cytosol during cell relaxation [1, 2, 3]. It has also been found that, at low ratios of dATP to ATP, large nonlinear increases in force are observed at physiological Ca^{2+} concentrations [4]. Therefore, upregulation of dATP in cardiac cells *via* adenoviral-mediated gene transfection of Ribonucleotide Reductase (R1R2) has been studied as a potential treatment for heart failure [5, 6]. A variety of *in-vitro* and animal studies have demonstrated efficacy and safety of modest increases of dATP as a treatment, but further study is needed to resolve the specific molecular mechanics by which dATP augments cardiac myocyte contraction [7].

dATP has been studied experimentally in skinned myofibrils, cells, and small animal models, but the specific combination of mechanisms by which dATP improves contractility is not yet known. As previously hypothesized by Nowakowski *et al.* [3], mechanisms of deoxy-ADP and -ATP may include altered: (1) nucleoside triphosphate-myosin affinity; (2) acto-myosin affinity; (3) phosphate release from myosin; and (4) nucleoside disphosphate release from post-powerstroke myosin [3, 8]. Although significant work has been done to probe individual crossbridge transitions using transient kinetic methods [9, 10, 11], it is difficult to definitively decouple the complex array of molecular interactions occurring at small spatial and temporal scales. Multiscale computational models are a helpful tool for integrating heterogeneous experimental data. A variety of model paradigms have been used to simulate the contractile biophysics of the sarcomere [12, 13, 14]. There are three properties that we consider to be important for understanding the effects of dATP on force development that should be integrated into a model: spatial thin filament cooperativity; explicit tracking of ATP throughout the crossbridge cycle; and competitive binding of ATP and dATP at different ratios.

Here we present a novel model of thin filament activation and crossbridge cycling to address three mechanistic questions about the effects of dATP on cardiac contractility: (1) To what degree are crossbridge cycling rates altered when myosin binds dATP rather than ATP? (2) Is the significant effect of dATP on steady-state force development at low ratios of dATP:ATP a result of nearest-neighbor cooperativity, or other factors? (3) How do altered

crossbridge cycling rates with dATP treatment result in faster twitch relaxation kinetics? To constrain and inform parameter estimation, atomistic Brownian dynamics simulations were used to estimate attachment rates of myosin binding to actin. These predictions permitted a unique combination of powerstroke and detachment rate parameters to be found that best match published steady-state and dynamic experimental measurements. Further analysis shows that nearest-neighbor interactions between regulatory units along the thin filament likely contribute to the significant increases in steady-state force outputs at low fractions of dATP, but do not fully explain experimental findings. We also concluded that observed alterations in twitch kinetics during dATP treatment are likely to depend, in part, on additional effects of dATP on the intracellular calcium transient.

2 Methods

2.1 Model Description

We constructed a Monte Carlo Markov Chain (MCMC) model of thin filament activation and crossbridge cycling which is based on the integration of two existing Monte Carlo models of the sarcomere [12, 15]. The model has a total of five states for each of 26 regulatory units (RUs) spaced evenly in one spatial dimension over time. Each RU consists of seven actin monomers, the troponin (Tn) complex, one tropomyosin (Tm) molecule, and the nearest available myosin S1 head. We assume that only one crossbridge (XB) may bind a single thin filament RU at a time as in earlier iterations of the model [16, 12].

An RU may occupy one of five possible conformational states at a given time. In state *B0*, the Tm molecule is fully covering the myosin binding site on the actin thin filament, constituting the “Blocked” state. Rates k_{Ca}^{+} and k_{Ca}^{-} govern the transition to state *B1* in which Ca^{2+} has bound to the Tn complex on the thin filament, allowing for a conformational change in Tn that allows Tm more flexibility. Rates k_{B}^{+} and k_{B}^{-} govern the transition to state *C* in which Tm moves 25 degrees azithumally into the “Closed” position on the thin filament, partially exposing the myosin binding site. The nearest myosin S1 head is detached from the thin filament. Rates k_{f}^{+} and k_{f}^{-} govern the transition to state *M1* in which myosin is bound to the thin filament, sliding Tm an additional 10 degrees into the “Open” state. The XB is in the pre-powerstroke state and does not produce force. Myosin is bound to ADP and Pi. Rates k_{p}^{+} and k_{p}^{-} govern the transition to state *M2* in which the XB is bound and in the post-powerstroke, force producing state, after Pi release. We refer to the k_{p}^{+} parameter as the powerstroke rate in the text, but this is a lumped parameter encompassing the powerstroke and Pi release. Finally, rates k_{g}^{+} and k_{g}^{-} allow RUs to transition back to the *C* state concurrently with ADP release and either repeat the XB cycle or relax back to the *B* states (Figure 1).

2.2 Thin filament activation kinetics and cooperativity

Thin filament cooperativity was introduced into the model in the same manner as previous studies [12, 16]. Briefly, we begin with the Gibbs relation to calculate an equilibrium

constant K_{BC}^{ref} between states B and C, in the case where both neighboring RUs are in the C state:

$$K_{BC}^{ref} = exp\frac{-\Delta G_{B\leftrightarrow C}^{ref}}{RT} \quad (1)$$

In the case where the nearest neighbors are in a state other than C, the transition to the C state will become less probable due to steric hindrance and Tm overlap. We represent the additional energy barriers due to the positions of nearest-neighbor Tm molecules, where X and Y represent the left and right neighbors, respectively, as:

$$\Delta G_{BC}^{XY} = \Delta G_{BC}^{ref} + \Delta G_{BC}^{X} + \Delta G_{BC}^{Y} \quad (2)$$

Therefore the equilibrium constant K for the transition from B to C with left and right neighbors in states X and Y, is calculated as

$$K_{BC}^{XY} = \gamma(XY)K_{BC}^{ref} \quad (3)$$

As derived previously [12], the cooperativity coefficients for all possible combinations of neighbor states are:

$$\gamma(XY) = \gamma(YX) = \begin{cases} \gamma_B^{-2} & B, B \\ \gamma_B^{-1} & B, C \\ \gamma_B^{-1}\gamma_M & B, M \\ 1 & C, C \\ \gamma_M & C, M \\ \gamma_M^2 & M, M \end{cases} \quad (4)$$

where

$$\gamma_B = \left(exp\frac{-\Delta G_{B\rightarrow C}^{B}}{RT}\right)^{-1} \quad (5)$$

and

$$\gamma_M = exp\frac{-\Delta G_{B\rightarrow C}^{M}}{RT} \quad (6)$$

Essentially, γ_B represents the cooperative impact of a neighboring blocked RU which tends to pull nearby RUs into the B state from the C state when $\gamma_B > 1$. γ_M then represents the impact of neighboring RUs on the M state, which facilitates the movement toward the M state if the value of $\gamma_M > 1$. Both γ_B and γ_M take into account cooperative mechanisms

owing to Tm overlap. The γ_M parameter also implicitly encompasses strain dependence, as crossbridge attachment further facilitates movement into the M state for nearest-neighbor RUs.

Coefficient q, which determines the weight of cooperative coefficient γ toward forward and reverse rates were set to $q = 1$ for all simulations, where q factors into dynamic simulations as:

$$k_{b+}^{XY} = k_{b+}^{ref}\gamma(XY)^{q} \tag{7}$$

$$k_{b-}^{XY} = k_{b-}^{ref}\gamma(XY)^{(q-1)} \tag{8}$$

The calcium binding step is not considered to be a cooperative process, and rates are calculated as:

$$k_{Ca}^{+} = k_{Ca}^{+ref} * \left[Ca^{2+}\right] \tag{9}$$

$$k_{Ca}^{-} = k_{Ca}^{-ref} \tag{10}$$

2.3 Crossbridge Cycling Kinetics

As described in previous studies [15, 17], the free energy of each crossbridge cycling state is defined as a function of XB distortion:

$$G_C = 0 \tag{11}$$

$$G_{M1} = \alpha\Delta G + k_{XB,RT}(x - x_{b0})^2 \tag{12}$$

$$G_{M2} = \eta\Delta G + k_{XB,RT}x^2 \tag{13}$$

Where constants $\alpha = 0.28$ and $\eta = 0.68$ as set in the original model [15], and ΔG represents free energy of ATP turnover. XB distortion in the *M1* state was considered to be 0, which simplifies the free energy profile for state *M1* to $G_{Ma} = \alpha\Delta G$. XB distortion in the *M2* state was assumed to be 7.5 nm. ΔG was determined as a function of concentrations of ATP, ADP, and Pi which were assumed to be constant for our system:

$$\Delta G = \Delta G_{ATP} - ln\left(\frac{[ATP]}{[ADP][Pi]}\right) \tag{14}$$

where [ATP] and [Pi] = 3 mM, [ADP] = 30 uM, and $\Delta G_{ATP} = 13$ RT.

In order to maintain detailed balance, reverse rates r_{ji} for XB transitions were calculated from forward rates r_{ij} through the following relationship :

$$\frac{r_{x,ij}(x)}{r_{x,ji}(x)} = e^{G_i(x) - G_j(x)} \tag{15}$$

where i is the initial state and j is the final state for a given transition. For example, to determine the reverse powerstroke rate, k_p^-, which represents the transition from the $M2$ state back to the $M1$ state,

$$k_P^- = \frac{k_P^+}{e^{G_{M1}(x) - G_{M2}(x)}} \tag{16}$$

As in the case of the B to C transition, the C to M transition is affected by nearest neighbor interactions due to the presence of myosin heads pushing the Tm molecule an additional 10 degrees around the filament. To represent the nearest neighbor interactions present in the C to $M1$ and C to $M2$ transitions, the equilibrium constant for the transition from C to M is

$$K_C M^{XY} = \mu(XY) K_C M^{ref} \tag{17}$$

and the coefficients $\mu(XY)$ are:

$$\mu(XY) = \mu(YX) = \begin{cases} \mu_B^{-2} & B, B \\ \mu_B^{-1} & B, C \\ \mu_B^{-1}\mu_M & B, M \\ 1 & C, C \\ \mu_M & C, M \\ \mu_M^2 & M, M \end{cases} \tag{18}$$

The coefficient r that determines the weight of cooperative coefficient μ toward M or C states was set to 1 for all simulations, where r enters into dynamic simulations as:

$$f^{+XY} = f^{+ref}\mu(XY)^r \tag{19}$$

$$f^{-XY} = f^{-ref}\mu(XY)^{(r-1)} \tag{20}$$

$$g^{+XY} = g^{+ref}\mu(XY)^{(r-1)} \tag{21}$$

$$g^{-XY} = g^{-ref}\mu(XY)^r \tag{22}$$

2.4 Monte Carlo Methods

The isometric model was simulated in time using Monte Carlo methods and implemented for fast execution on a GPU using CUDA. The probability of a given transition p_{ij} at a given time step was calculated as:

$$p_{ij} = r_{ij}\Delta t \tag{23}$$

where r_{ij} is the reaction rate considering the state of the left and right neighboring RUs and Δt is the chosen time step. At each time step, for each RU, a random number R between 0 and 1 was generated, and transitional probabilities were calculated for the given RU considering its current state and the states of neighboring RUs. Potential transitions were calculated for each state based on Figure 1. For example, in the case where a given RU is in the *M1* state, with a left neighbor in the *B0* state and right neighbor in the *C* state,

$$P1 = k_P^+\Delta t \tag{24}$$

$$P2 = f^-(BC)\Delta t \tag{25}$$

The final state of the RU, $Z_{t+\Delta t}$, is determined by comparing R to P1 and P2. If $R < P1$, $Z_{t+\Delta t} = M2$. If $P1 < R < (P1 + P2)$, $Z_{t+\Delta t} = C$. If $(P1 + P2) < R$, $Z_{t+\Delta t} = M1$, in other words, the RU does not change states. A timestep of $\Delta t = 5e^{-4}$ ms was chosen for the simulations. As investigated in previous versions of the model, this step size was necessary to ensure that all transition probabilities for a given state, when multiplied by timestep and summed, do not approach or exceed 1 [12, 16].

For steady state simulations, constant $[Ca^{2+}]$ was applied for all t. The initial condition for all 26 RUs is the *B0* state, and boundary conditions were set so that the 1st and 26th RU were clamped in the B0 state. The proportion of RUs in each state was recorded at each time step. Simulations were repeated a minimum of 1000 times and state occupancy averaged due to the stochasticity of the system. Total force was considered to directly relate to the number of RUs in the *M2* state at any time t. Therefore, to calculate steady state force F_{SS}, the number of RUs in the *M2* state for all $2.5 < t < 3.0s$ were averaged, and normalized to the value at $pCa = 4.0$ (Figure 1 B–D).

To simulate slack-restretch experiments for the calculation of rate of tension redevelopment (k_{tr}), a steady-state simulation is run for 2 s to achieve steady state force, at which point all RUs are reset to state B1 to simulate breaking of XBs. Then, the steady state simulation continues to allow maximum steady state force to redevelop and k_{tr} is calculated as $k_{tr} = (1.264t_{1/2})^{-1}$ [18] in order to compare with experimental values which were calculated in the same manner [19].

Simulations were performed with varying ratios of dATP to ATP in order to test competitive binding of the nucleotide. The association rate of ATP and dATP to myosin were assumed to be identical due to earlier studies suggesting the same [1]. For each RU moving from the *C* state to the *M* state, an additional random number P was generated at each time point. This

number was compared to the inputted percent dATP of the system. If $P >$ percent$_{dATP}$, the ATP rates were used to govern the transition. However, if $P \leq$ percent$_{dATP}$, dATP was considered to be bound to myosin instead and dATP rates were used for the transition. A boolean was used to track the presence of ATP/ADP (0) or dATP/dADP (1) attached to myosin in both the *M1* and *M2* states depending on the nucleotide present during the tropomyosin transition from *C* to *M*.

2.5 Parameter selection and optimization

Wild type (WT) steady state force values at various Ca^{2+} concentrations were optimized to experimental data from Regnier et al. [19], who measured steady-state force in skinned rat trabeculae (male Sprague-Dawley rats, 200–250 grams) with the α-myosin heavy chain (α-MHC) isoform and varying [ATP] in the system. It was also assumed that $\gamma_B > \gamma_M > \mu_M$ as in previous studies because the energy required to move Tm 25 degrees from the *C* to *B* state is assumed to be higher than the smaller 10-degree *C* to *M* transition [12]. Optimized parameters are displayed on the first line of Table 1. Optimization was further constrained by matching the experimental slack-restretch rate of tension redevelopment (k_{tr}) at pCa = 4.0, which was measured to be 13.8 s^{-1}.

The value of k_{Ca}^{+} was set to 0.09 $\mu M^{-1} ms^{-1}$ based on experimental FRET studies of Tn-Tm complexes in rats [20]. k_f^{+} was set to 0.0025 $\mu M^{-1} ms^{-1}$ based on various experimental measurements of acto-myosin association [21, 22]. Other model parameters were optimized to minimize a combined root mean square error of 9 steady state force data points and a single k_{tr} value, and are summarized in Table 1. The corresponding steady state output values are visualized as the black curve in Figure 3A.

In this study, we used the particle swarm optimization (PSO) technique [23] to find the optimal values of the model parameters. This particular fitting algorithm belongs to a population search class of optimization methods, which is normally used to improve a candidate solution with regard to a given quality measure. The PSO algorithm starts by distributing initial particles (random values assigned to each model parameters), which are normally known as solution candidates. These solution candidates are also assigned initial velocities. An objective function for each particle location is then formed to determine the lowest function value and the “best” position. New velocities are then computed using the current velocity, the particles’ individual best locations, and the best locations of their neighbouring candidates. The process is repeated iteratively until the algorithm reaches the desired stopping accuracy criterion. More details about the PSO method can be found in [24].

2.6 Brownian dynamics

Brownian Dynamics studies were used to quantify the change in acto-myosin association rate due to dATP treatment. Methods for the simulations drawn from herein are described in detail in [25] and illustrated in Figure 2A. PDB: 5KG8 was used as a template structure for the bound conformation of myosin and an actin dimer [26] (Figure 2B). The template structure 5KG8 represents Myosin X binding to the actin thin filament, which is a different isoform than the one used in our simulations, but the template was used only to orient

myosin and actin in an approximate bound conformation for the purpose of simulation setup. ADP- and dADP- bound myosin S1 structures were gathered from run 1 of molecular dynamics simulations from Nowakowski *et. al.* [8] at 50 ns. PQR files were created for all structures using the Amber18 forcefield with PDB2PQR [27, 28, 29]. Electrostatic fields were generated for both myosin and actin structures using APBS [30].

To determine association rates, Brownian dynamics (BD) simulations were performed using BrownDye software [31] (Figure 2A). For each trajectory, BrownDye spawns the myosin molecule at a random position on a sphere at radius b from the actin dimer. A combination of Brownian motion and intermolecular forces (electrostatics and short range forces) determine whether the molecules move closer together, to within the set reaction distance, or separate to a farther q orbit and escape from each other. 500,000 trajectories were completed for both ADP-and dADP myosin association with an actin dimer. For each trajectory, a binding event was considered to occur if three atom pairs (calculated as likely hydrogen bonding atoms within 3.5 Å of each other in the bound conformation) moved within a certain reaction distance during the trajectory. The distance criterion was tested by performing spot checks of 25 random association trajectories to ensure that association events captured the correct alignment of the molecules. Instead of prescribing a specific reaction distance for the simulation, the closest distance between the binding regions was recorded for each trajectory. This allowed for calculation of association rates for a wide range of reaction distances (6 Å to 100 Å) using the *rates_of_distances* function in BrownDye. For more detailed information on BD methods and rate calculation, see [25].

3 Results

3.1 Brownian dynamics studies quantify increased XB attachment rate for dATP-myosin

After optimizing the model for the WT ATP case, attempts were made to match the experimental dATP data by altering just three parameters: k_f^+ (XB attachment), k_p^+ (powerstroke rate), and k_g^+ (XB detachment). These three parameters were chosen because they are transition points that directly involve ATP and its interaction with myosin S1 [17]. As hypothesized previously [1, 3], our initial assumption was that all three forward XB parameters should be increased to lead to higher force production and faster XB cycling. For the purposes of our model, we also assumed that these three parameter changes should be sufficient to explain all changes in crossbridge behavior as a result of dATP treatment. Brownian dynamics simulations of myosin-actin association showed a significant increase in XB association rate for all measured reaction distances [25]. Our assumed value for k_f^+ in an all-ATP system (0.0025 ms^{-1}) constrains the BD study to a reaction distance of 8.28 Å. A local myosin concentration of 1 μM was assumed in order to convert the second order association rate to the first-order k_f^+. If we assume a quasi-steady state among the crossbridge states, and that k_f^- remains the same from ATP to dATP, then the exact value of this myosin concentration should have no effect on the results. Using the same reaction distance in order to provide an accurate rate comparison, BD simulations predicted that

dATP increases the association rate k_f^+ (XB attachment) 2.3-fold to 0.00567 ms^{-1} (Figure 2C).

The results show a clear increase in XB attachment when dATP is bound to myosin rather than ATP. This is consistent with previous hypotheses that dATP increases force by increasing XB attachment rate. For the range of reaction distances 7 Å to 10 Å, fold change between ATP myosin and dATP myosin ranges between 2.2 and 2.8, indicating relatively stable effect of dATP on the system for this physiological range, even if a different wildtype association rate were to be chosen.

3.2 dATP increases maximum steady state force and Calcium sensitivity

Considering a single calculated k_f^+ determined directly from BD simulations, we attempted to recreate experimental steady state and dynamic data in a dATP system by altering k_p^+ and k_g^+. Initial attempts were made to match kinetics by altering solely k_g^+, but this did not allow us to represent an accurate increase in k_{tr} (see Figure S1). Accurate recreation of both steady state and slack-restretch experimental data requires an increase in both maximum force and calcium sensitivity, in other words, a combination of increases in k_p^+ and k_g^+, in order to attain low residual values for both steady state and k_{tr} data.

After optimizing for k_p^+ and k_g^+, the dATP experimental steady state data could indeed be reliably recreated with a unique set of XB parameters (Figure 3). A combination of $k_p^+ = 0.08\,ms^{-1}$, a 60% increase, and $k_g^+ = 0.23\,ms^{-1}$, an 70% increase, minimized the residual compared to experimental dATP data. The best fits to the experimental steady-state force-pCa curves can be seen in Figure 3A. The maximum force is higher than experimental values, but the overall residual is 0.15 and k_{tr} matches the experimentally calculated value of 17.6 s^{-1} exactly.

At pCa = 4.0, experiments determined k_{tr} = 13.8 s^{-1} for the ATP case and 17.6 s^{-1} for the dATP case, a 27.5% increase [19]. In our simulations, k_{tr} = 13.4 s^{-1} for ATP and 17.6 s^{-1} for dATP, a 31% increase. The simulated k_{tr} experiments are displayed in Figure 3B and C, visualized to demonstrate change in maximum force (Figure 3B) and tension redevelopment kinetics (Figure 3C) in the separate images. The experimental k_{tr} values are remarkably close to the simulated values, with error in the ATP case of 0.4 s^{-1} or 2.9%. Although it was possible to more closely match steady state experimental results by lowering k_p^+ to 0.03 ms^{-1}, this parameter change led to lower k_{tr} than the ATP case which is nonphysiological (see Figure S2). A sensitivity analysis of rates k_p^+ and k_g^+ was performed in order to test effects on maximum force and calcium sensitivity for each of the two rates on steady state behavior, and is shown in Figure S1.

3.3 Nonlinear force increases are observed at low dATP/ATP ratios

Steady-state simulations were performed on the system at various ratios of dATP to ATP with competitive nucleotide binding. In Figure 4 the steady state force is displayed for various dATP percents at pCa = 5.5 and pCa = 4.0 to allow for qualitative comparisons to

experimental studies in skinned pig trabeculae [4]. Exaggerated nonlinear increases are seen at very low dATP levels at both pCa 4.0 and 5.5 (Figure 4, black lines). For example, at 10% dATP, an overall 34% increase in force is apparent at pCa 4.0, and a 27% increase at pCa 5.5. Even when thin filament cooperativity is not included in the model (all cooperative parameters = 1, no coupling between RUs) nonlinear increases are still seen due to the overwhelming effects of the large rate increases on overall XB cycling speed and force production. For example, at 10% dATP, the force increase without coupling is 32% at pCa 4.0, and 24% at pCa 5.5.

At both pCa values, the nonlinearity of the relationship is decreased slightly when RU-RU coupling is removed from the model. At the therapeutic 5% dATP value with RU-RU coupling, 19.1% of maximal force development is acheived. A slightly smaller effect was seen with no RU-RU coupling. At 5% dATP, only 13.3% of the total dATP force increase is observed. We still see a nonlinear response, but the effect is less pronounced without coupling of RUs. The most pronounced effect of RU coupling is instead apparent in maximum force development. For the 4.0 pCa, 0% dATP case, without RU coupling the steady state force was just 27.3% of the force in the full model, although the figure has been normalized to demonstrate nonlinearity more clearly.

3.4 dATP enhances twitch kinetics

Twitch simulations were performed by inputting calcium transients measured in adult rat cardiomyocytes paced at 0.5 Hz by Korte *et al.* [2] into the model and observing force outputs. The input transients are visible in insets of Figure 5. First, the untreated calcium transient was tested on varying ratios of dATP to ATP in the XB model. Increasing dATP percent led to increased maximum twitch force, with the 100% dATP case resulting in a 48% increase in maximum twitch force compared to WT. At 25% dATP, the maximum force increase was 35% of the full dATP gain, again outputting higher force increases at low dATP levels than one would expect if the relationship between F_{max} and dATP % were linear. Interestingly, the relaxation time to 50% force (RT_{50}) was increased from 68.5 ms to 76 ms in the 100% dATP case compared to WT (5B). As for the time to 90% relaxation (RT_{90}), in the 100% dATP case RT_{90} = 144 ms, a decrease compared to the ATP case where RT_{90} = 162 ms. In the original experiments, these values both decreased with dATP treatment. A direct value comparison isn't possible, however, because the experiments measured shortening in intact cells, whereas our model simulates isometric skinned trabeculae.

During the experiments, an altered calcium transient was also observed in the case of dATP treatment. When the WT calcium transient was input to generate WT force and the dATP calcium transient was used for the 100% dATP twitch, RT_{50} decreased to 42 ms (5C) in the dATP case. RT_{90} also decreased in the dATP case to 86 ms from the WT value of 162 ms. This result suggests that experimentally observed altered twitch kinetics during dATP therapy owe in part to effects of the treatment on intracellular calcium handling. Further study should be pursued on the effect of dATP on the ATP-dependent Ca^{2+} pumps, especially the sarcoendoplasmic reticulum Ca^{2+}-ATP-ase, SERCA.

4 Discussion

In this study, we used a multi-scale computational modeling approach to gain insight into the mechanisms by which 2-deoxy-ATP, even in low quantities compared to ATP, can significantly increase myocyte twitch force, thin filament calcium sensitivity, and twitch force kinetics. Using atomistic Brownian dynamics simulations, we predicted significant increases in the attachment rate of dADP-myosin to actin than ADP-myosin. In alignment with a previous study combining electrostatic analysis of the myosin-actin binding surface and x-ray diffraction experiments, the increase in attachment rate is likely due to electrostatic changes to the myosin surface after dATP binding [25]. These results then constrained the parameter estimation of a Markov-state model of cooperative myofilament interactions so that unique estimates of the crossbridge dissociation and power-stroke kinetics could be obtained from previously measured steady-state force-calcium and tension redevelopment measurements in rat trabeculae. These optimizations suggested that the attachment rate increase predicted by BD simulations of myosin association to an actin (2.3 fold), combined with modest increases in both the powerstroke and XB detachment rate (60% and 70%, respectively), reliably reproduce tension development and steady state experimental results. The increase in duty cycle (due to a larger increase in attachment than detachment rate) contributes to the observed force increases in steady state results, as originally predicted in experimental studies which stated that increases to k_f^+ must be higher than increases to k_g^+ [19]. In comparing slack-restretch simulation results to experimental data (Figure 3B), relative error was calculated using the k_{tr} value rather than specific experimental data points. This method of comparison was chosen due to variance in individual experiments, and our 31% increase in k_{tr} is within the bounds established during the experimental study (27 ± 5%) [19].

An interesting finding regarding the therapeutic potential of dATP is that relatively large force increases have been observed even at small dATP/ATP ratios [2, 3, 32]. Using the optimized dATP XB cycling rates, our model predicts that a positive nonlinear force increase occurs in steady state cases, with 19.1% of potential steady state force increase occurring at just 5% dATP in a Ca^{2+}-rich environment (pCa = 4.0). In an experimental study on pig trabeculae, nonlinear increases in steady-state force were observed between 0% dATP and 20% dATP at pCa 5.5 but force increases were relatively linear compared to dATP concentration at pCa 4.0 [4]. Our study demonstrated a nonlinear pattern at all pCa values, even without RU-RU coupling present. Our initial hypothesis was that the observed pattern occurs due to thin filament cooperativity, as a small number of bound dATP XBs could precipitate thin filament activation of neighboring RUs. Without RU coupling, the nonlinear effects are less pronounced in our model. However, there are other factors at play which must contribute to the positive nonlinearity apparent even without coupling. One potential contributor may be the increase in XB cycling speed and duty cycle of dATP-bound XBs. From the two-actin BD simulation, k_f^+ increased 2.3-fold and k_g^+ was increased by 60%. This larger increase in attachment rate compared to detachment leads to a greater overall M state occupancy in the dATP case. At any given time during dATP-aided XB cycling, XBs are more likely to be attached, which may have an outsize effect on overall force production. Further experimental study of this phemonenon in rat cardiomyocytes would allow for a

more definite conclusion. Although our model replicates the overall positive nonlinear phenomenon, there were quantitative differences between our model results and experimental results in the pig studies [4]. This discrepancy may be due to species differences. Pig muscle experiments test cardiac muscle with β-MHC as the dominant isoform, whereas our model is optimized for rats expressing α-MHC. In fact, an experimental study testing differences between the effects of dATP on α- and β-MHC demonstrated varied impact on steady state and developing force between the isoforms [19].

The model described in this work also makes predictions about alterations to twitch kinetics due to dATP treatment. Positive nonlinear increases in steady state forces are observed in twitch simulations, indicating that low therapeutic levels of dATP can provide significant increases in cardiac contractility in physiological scenarios. Interestingly, when providing the WT calcium transient in all simulations, the model increases maximum force as the percent dATP increases, but relaxation slows as indicated by RT_{50}. This result seems to be in opposition to experimental *in-vivo* results in various species displaying improved relaxation kinetics. However, when using dATP- affected calcium transients gathered from experimental data [2], accelerated relaxation rates were indeed observed in the model, both in RT_{50} and RT_{90}. Therefore, an integrated model of excitation-contraction coupling should be employed to further explore mechanisms by which dATP alters the complex feedback web between the sarcomere, in a dual role as force producer and calcium buffer, and calcium handling ATPases such as PMCA, SERCA, and NCX.

It should be noted that the BD system used in this study to measure the role of differing electrostatic interactions on the association rate between actin and myosin was simplified. We considered a free floating myosin S1 and two actin molecules rather than myosin as part of a much larger thick filament system and a thin filament containing dozens of actin monomers as well as other thin filament proteins such as troponin, tropomyosin, and myosin binding protein C. However, we chose to model the actin-myosin interaction in a simplified system in order to study the specific effects of dATP on the kinetics before integrating into a larger-scale model which incorporates other thin filament proteins such as troponin. The ability of this simplified system to predict a reasonable change in myosin attachment rate is evidence of the significant role that electrostatic acto-myosin interactions have in the differences between observed attachment rate for ATP- and dATP- myosin. Further molecular study should be pursued to validate the accuracy of the specific rate constants, e.g. the 60% increase in powerstroke rate and 70% increase in detachment rate resulting from dATP binding predicted by our model.

The Markov State model used in our study, although chosen for spatial tracking of RUs and simple manipulation of cooperativity coefficients, remains limited in applicability. For example, the model currently has isometric-only functionality, and does not explicitly factor in strain dependent mechanisms. We also do not account for filament compliance or the possibility that multiple S1 heads may bind to a single RU, which is a strength of other models [33, 15]. Another assumption made for model simplicity is that movement of Tm into the M state is necessarily coincident with XB attachment, which may not be valid in all circumstances [34]. The assumptions made allowed us to answer a limited range of questions about isometric experimental data, but future work should investigate shortening

capability and integration with other cellular processes such as metabolism and calcium handling. Our findings also require further experimental validation to ensure that our predictions about isometric twitch kinetics and nonlinear steady state force increases at low dATP treatment levels are indeed correct. Despite the lack of existing experimental data in intact cardiac muscle that would allow a 1-to-1 comparison for the twitch simulations presented in Figure 5, there are comparable experimental results in ventricular function [35, 36, 5, 6] which gave us confidence in our findings.

Our results strengthen the hypothesis that the mechanism of dATP therapy, with regard to improvements in crossbridge function, is largely based on acto-myosin interaction. Increasing cardiac dATP does not affect cooperative mechanisms directly, but rather conformationally alters myosin so that it has an increased affinity to the actin thin filament when detached, coupled with an increased tendency to detach from actin when in the post-powerstroke state. We also considered the possibility that an altered myosin S1 conformation may lead to a faster powerstroke. Our results show that with these constraints on a Markov Chain model of the sarcomere, we can reliably reproduce isometric experimental results regarding the effects of dATP therapy on steady state force production and tension development kinetics. The experimentally observed improvement in twitch relaxation during dATP treatment was hypothesized to occur due to increased XB detachment rate. Indeed, our optimization, after taking into account the increased attachment rate predicted by BrownDye, concluded that a XB detachment rate of 70% is required to match kinetic and steady state experimental results. We recommend further study to investigate the effects of dATP on calcium reuptake, through a combination of increased calcium buffering on the thin filament and dATP interactions with Ca^{2+}-ATPases. Using our multiscale framework of integration from atomistic scale to a Monte Carlo Markov Chain model of sarcomere mechanics, we have quantified the electrostatic effects of dATP on myosin-actin association and investigated the impact of dATP on sarcomere force development.

Supplementary Material

Refer to Web version on PubMed Central for supplementary material.

Acknowledgements

This work was supported by the National Institutes of Health [grant numbers P41GM103426, T32 HL 105373, U01 HL122199, R01 HL137100, GM31749, R01 HL128368 and RM1GM131981]. K.J.M is supported by the Simula-UCSD-University of Oslo Research and PhD training (SUURPh) programme, an international collaboration in computational biology and medicine funded by the Norwegian Ministry of Education and Research.

References

[1]. Regnier M, Rivera AJ, Chase PB, 2-deoxy-ATP enhances contractility of rat cardiac muscle, Circ Res 86 (2000) 1211–1217. [PubMed: 10864910]

[2]. Korte FS, Dai J, Buckley K, Feest ER, Adamek N, Geeves MA, Murry CE, Regnier M, Upregulation of cardiomyocyte ribonucleotide reductase increases intracellular 2 deoxy-ATP, contractility, and relaxation, J Mol Cell Cardiol 51 (6) (2011) 894–901. [PubMed: 21925507]

[3]. Nowakowski SG, Kolwicz SC, Korte FS, Luo Z, Robinson-Hamm JN, Page JL, Regnier M, Transgenic overexpression of ribonucleotide reductase improves cardiac performance, Proceedings of the National Academy of Sciences 110 (15) (2013) 6187–6192.

[4]. Schoffstall B, Clark A, Chase PB, Positive inotropic effects of low dATP/ATP ratios on mechanics and kinetics of porcine cardiac muscle, Biophys J 91 (6) (2006) 2216–2226. [PubMed: 16798797]

[5]. Thomson KS, Odom GL, Murry CE, Mahairas GG, Moussavi-Harami F, Teichman SL, Chen X, Hauschka SD, Chamberlain JS, Regnier M, Translation of cardiac myosin activation with 2-deoxy-ATP to treat heart failure via an experimental ribonucleotide reductase-based gene therapy, Biophys J 1 (7) (2016) 666–679.

[6]. Kadota S, Carey J, Reinecke H, Leggett J, Teichman S, Laflamme M, Murry CE, Regnier M, Mahairas GG, Ribonucleotide reductase-mediated increase in dATP improves cardiac performance via myosin activation in a large animal model of heart failure, Eur J Heart Fail 17 (8) (2015) 772–81. [PubMed: 25876005]

[7]. Teichman SL, Thomson KS, Regnier M, Cardiac myosin activation with gene therapy produces sustained inotropic effects and may treat heart failure with reduced ejection fraction, Handb Exp Pharmacol 243 (2017) 447–464. [PubMed: 27590227]

[8]. Nowakowski SG, Regnier M, Daggett V, Molecular mechanisms underlying deoxy-ADP. Pi activation of pre-powerstroke myosin, Protein Sci 26 (4) (2017) 749–762. [PubMed: 28097776]

[9]. Málnási-Csizmadia A, Pearson DS, Kovács M, Woolley RJ, Geeves MA, Bagshaw CR, Kinetic resolution of a conformational transition and the atp hydrolysis step using relaxation methods with a dictyostelium myosin ii mutant containing a single tryptophan residue, Biochemistry 40 (42) (2001) 12727–12737. [PubMed: 11601998]

[10]. Mijailovich SM, Nedic D, Svicevic M, Stojanovic B, Walklate J, Ujfalusi Z, Geeves MA, Modeling the actin. myosin atpase cross-bridge cycle for skeletal and cardiac muscle myosin isoforms, Biophysical journal 112 (5) (2017) 984–996. [PubMed: 28297657]

[11]. Cremo CR, Geeves MA, Interaction of actin and adp with the head domain of smooth muscle myosin: implications for strain-dependent adp release in smooth muscle, Biochemistry 37 (7) (1998) 1969–1978. [PubMed: 9485324]

[12]. Campbell SG, Lionetti FG, Campbell KS, McCulloch AD, Coupling of adjacent tropomyosins enhances cross-bridge-mediated cooperative activation in a markov model of the cardiac thin filament, Biophys J 98 (2010) 2254–2264. [PubMed: 20483334]

[13]. Land S, Niederer SA, A spatially detailed model of isometric contraction based on competitive binding of troponin i explains cooperative interactions between tropomyosin and cross-bridges, PLoS Comput. Biol 11 (2015) e1004376. [PubMed: 26262582]

[14]. Rice JJ, Wang F, Bers DM, de Tombe PP, Approximate model of cooperative activation and crossbridge cycling in cardiac muscle using ordinary differential equations, Biophys J 95 (5) (2008) 2368–90. [PubMed: 18234826]

[15]. Tanner BC, Daniel TL, Regnier M, Sarcomere lattice geometry influences cooperative myosin binding in muscle, PLoS computational biology 3 (7) (2007) e115. [PubMed: 17630823]

[16]. Aboelkassem Y, Bonilla JA, McCabe KJ, Campbell SG, Contributions of Ca2+-independent thin filament activation to cardiac muscle function, Biophys J 109 (2015) 2101–2112. [PubMed: 26588569]

[17]. Pate E, Cooke R, A model of crossbridge action: The effects of ATP, ADP, and Pi, J Muscle Res Cell Motil 10 (1989) 181–196. [PubMed: 2527246]

[18]. Chase PB, Martyn DA, Hannon JD, Isometric force redevelopment of skinned muscle fibers from rabbit activated with and without Ca2+, Biophys J 67 (1994) 1994–2001. [PubMed: 7858136]

[19]. Regnier M, Martin H, Barsotti RJ, Rivera AJ, Martyn DA, Clemmens E, Cross-bridge versus thin filament contributions to the level and rate of force development in cardiac muscle, Biophys J 87 (3) (2004) 1815–1824. [PubMed: 15345560]

[20]. Dong W, Jayasundar JJ, An J, Xing J, Cheung HC, Effects of PKA phosphorylation of cardiac troponin I and strong crossbridge on conformational transitions of the n-domain of cardiac troponin C in regulated thin filaments, Biochemistry 46 (34) (2007) 9752–9761. [PubMed: 17676764]

[21]. Geeves MA, Dynamic interaction between actin and myosin subfragment 1 in the presence of ADP, Biochemistry 28 (14) (1989) 5864–5871. [PubMed: 2528376]

[22]. White HD, Taylor EW, Energetics and mechanism of actomyosin adenosine triphosphatase, Biochemistry 15 (26) (1976) 5818–5826. [PubMed: 12793]

[23]. Kennedy J, Eberhart R, Particle swarm optimization, Proceedings of the IEEE International Conference on Neural Networks (1995) 1942–1945.

[24]. Mezura-Montes E, Coello CAC, Constraint-handling in nature-inspired numerical optimization: Past, present and future, J. Swarm Evol. Comput (2011) 173–194.

[25]. Powers JD, Yuan C, McCabe KJ, Murray JD, Childers MC, Flint G, Moussavi-Harami F, Mohran S, Castillo R, Zuzek C, Ma W, McCulloch AD, Irving TC, Regnier M, Cardiac myosin activation with 2-deoxy-atp via increased electrostatic interactions with actin, Proceedings of the National Academy of Sciences 116 (23) (2019) 11502–11507.

[26]. Ropars V, Yang Z, Isabet T, Blanc F, Zhou K, Lin T, Liu X, Hissier P, Samazan F, Amigues B, Yang ED, Park H, Pylypenko O, Cecchini M, Sindelar CV, Sweeney HL, Houdusse A, The myosin X motor is optimized for movement on actin bundles, Science 7 (2016) 12456.

[27]. Case DA, Ben-Shalom IY, Brozell SR, Cerutti DS, Cheatham TE, Cruzeiro VWD, Darden TA, Duke RE, Ghoreishi D, Gilson MK, Gohlke H, Goetz AW, Greene D, Harris R, Homeyer N, Izadi S, Kovalenko A, Kurtzman T, Lee TS, LeGrand S, Li P, Lin C, Liu J, Luchko T, Luo R, Mermelstein D, Merz K, Miao Y, Monard G, Nguyen C, Nguyen H, Omelyan I, Onufriev A, Pan F, Qi R, Roe DR, Roitberg A, Sagui C, Schott-Verdugo S, Shen J, Simmerling CL, Smith J, Salomon-Ferrer R, Swails J, Walker RC, Wang J, Wei H, Wolf RM, Wu X, Xiao L, York DM, Kollman PA, AMBER 2018, University of California, San Francisco.

[28]. Dolinsky TJ, Nielsen JE, McCammon JA, Baker NA, PDB2PQR: an automated pipeline for the setup of Poisson-Boltzmann electrostatics calculations, Nucleic Acids Res 32 (2004) W665–7. [PubMed: 15215472]

[29]. Dolinsky TJ, Czodrowski P, Li H, Nielsen JE, Jensen JH, Klebe G, Baker NA, PDB2PQR: expanding and upgrading automated preparation of biomolecular structures for molecular simulations, Nucleic Acids Res 35 (2007) W522–5. [PubMed: 17488841]

[30]. Baker N, Sept D, Joseph S, Hoist M, McCammon JA, Electrostatics of nanosystems: Application to microtubules and the ribosome, Proc. Natl. Acad. Sci 98 (18) (2001) 10037–10041. [PubMed: 11517324]

[31]. Huber GA, McCammon JA, Browndye: A software package for brownian dynamics, Computer Physics Communications 181 (11) (2010) 1896–1905. doi:10.1016/j.cpc.2010.07.022. [PubMed: 21132109]

[32]. Moussavi-Harami F, Razumova MV, Racca AW, Cheng Y, Stempien-Otero A, Regnier M, 2-deoxy adenosine triphosphate improves contraction in human end-stage heart failure, Journal of molecular and cellular cardiology 79 (2015) 256–263. [PubMed: 25498214]

[33]. Williams CD, Regnier M, Daniel TL, Elastic energy storage and radial forces in the myofilament lattice depend on sarcomere length, PLoS Comput Biol 8 (11) (2012) e1002770. [PubMed: 23166482]

[34]. Lehrer SS, Geeves MA, The myosin-activated thin filament regulatory state, m-open: a link to hypertrophic cardiomyopathy (hcm), Journal of muscle research and cell motility 35 (2) (2014) 153–160. [PubMed: 24740688]

[35]. Kolwicz SC, Hall JK, Moussavi-Harami F, Chen X, Hauschka SD, Chamberlain JS, Regnier M, Odom GL, Gene therapy rescues cardiac dysfunction in duchenne muscular dystrophy mice by elevating cardiomyocyte deoxy-adenosine triphosphate, JACC: Basic to Translational Science 4 (7) (2019) 778–791. [PubMed: 31998848]

[36]. Kolwicz SC Jr, Odom GL, Nowakowski SG, Moussavi-Harami F, Chen X, Reinecke H, Hauschka SD, Murry CE, Mahairas GG, Regnier M, Aav6-mediated cardiac-specific overexpression of ribonucleotide reductase enhances myocardial contractility, Molecular Therapy 24 (2) (2016) 240–250. [PubMed: 26388461]

[37]. Humphrey W, Dalke A, Schulten K, VMD - visual molecular dynamics, J Molec Graphics 14 (1) (1996) 33–38.

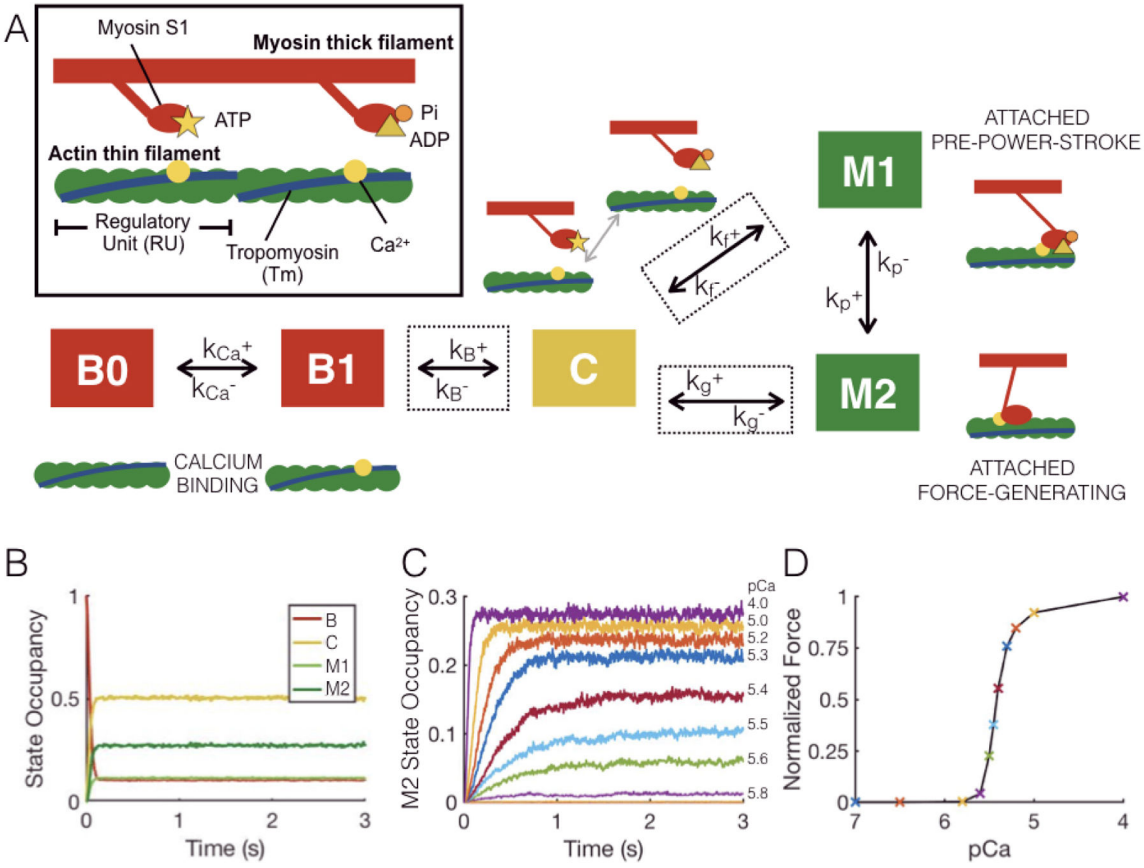

Figure 1:

(A) Schematic outlining the 5 main states of the Monte Carlo Markov Chain model. States *B0* and *B1* (red boxes) represent the blocked state of Tm, where 0 represents no Ca^{2+} bound and 1 represents bound Ca^{2+}. The *C* state (yellow box) represents a 25 degree azithumal shift in Tm around the actin filament to comprise the closed state. The green boxes represent the two states where Tm is in the Open state, a 35 degree total shift from the blocked state. *M1* represents the pre-powerstroke attached myosin position, and *M2* represents the post-powerstroke force producing condition. Transitions from Blocked to Closed to Open states are affected by nearest-neighbor Tm interactions, which is signified by the dotted lines surrounding the transition arrows. (B) For a single steady-State simulation, 1000 3-second timecourses are run and averaged at each pCa value being tested and occupancy of each state is tracked. (C) *M2* state occupancy is considered to be directly related to overall force production. The steady-state *M2* occupancy at each pCa value is calculated by averaging the final 0.5 s of the simulation. (D) Steady state values of force are normalized to the pCa 4.0 force output and plotted as a function of pCa.

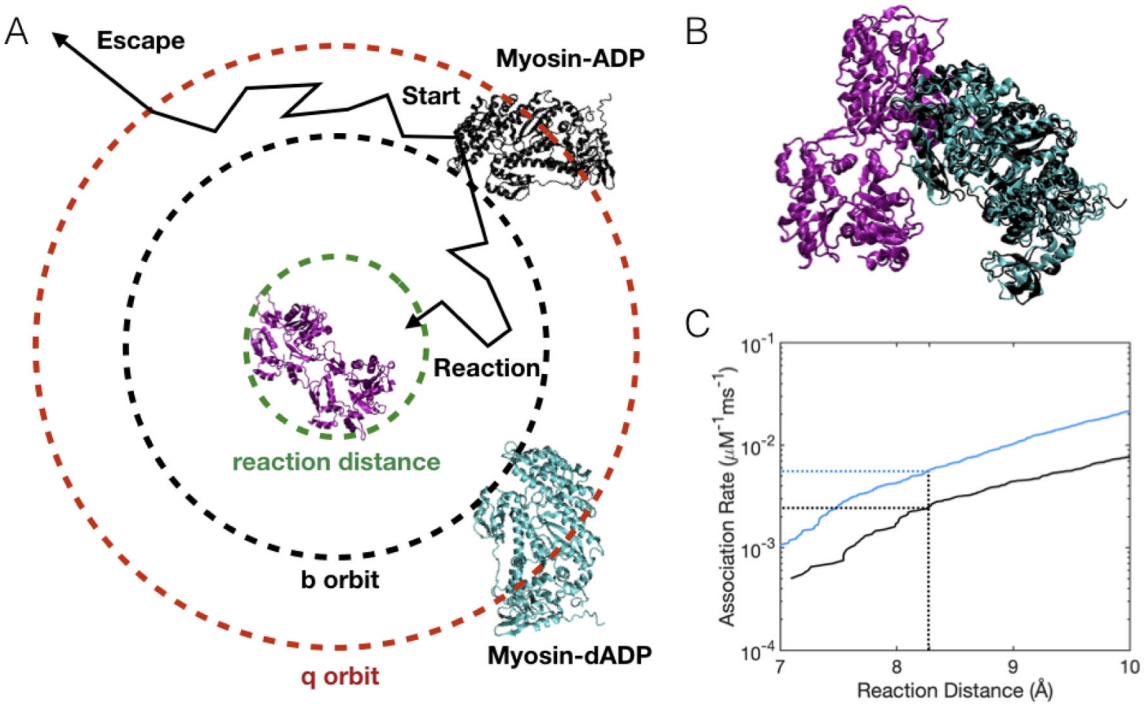

Figure 2:

BrownDye simulations of acto-myosin association were performed to determine the electrostatically-based differences in association rate between ADP- and dADP-bound myosin. A. For each BrownDye trajectory, a myosin monomer was generated randomly on a spherical surface approximately 120 Å from the actin dimer. A timecourse was run on the molecules combining random diffusion and electrostatic forces to determine if the molecules moved close enough to be within the prescribed reaction distance, or if the molecules moved farther away to the q radius and escaped. B. The bound conformation of ADP-myosin (black) or dADP-myosin (cyan) with an actin dimer, visualized using VMD [37]. C. Plot of second-order association rates for actin-myosin binding as a function of prescribed reaction distance. For WT simulations, the association rate was optimized to 0.0025 ($\mu M^{-1} ms^{-1}$) which corresponds to a reaction distance of 8.28 Å. Using the same reaction distance, the dATP actin-myosin association rate is determined to be 0.00567 ($\mu M^{-1} ms^{-1}$).

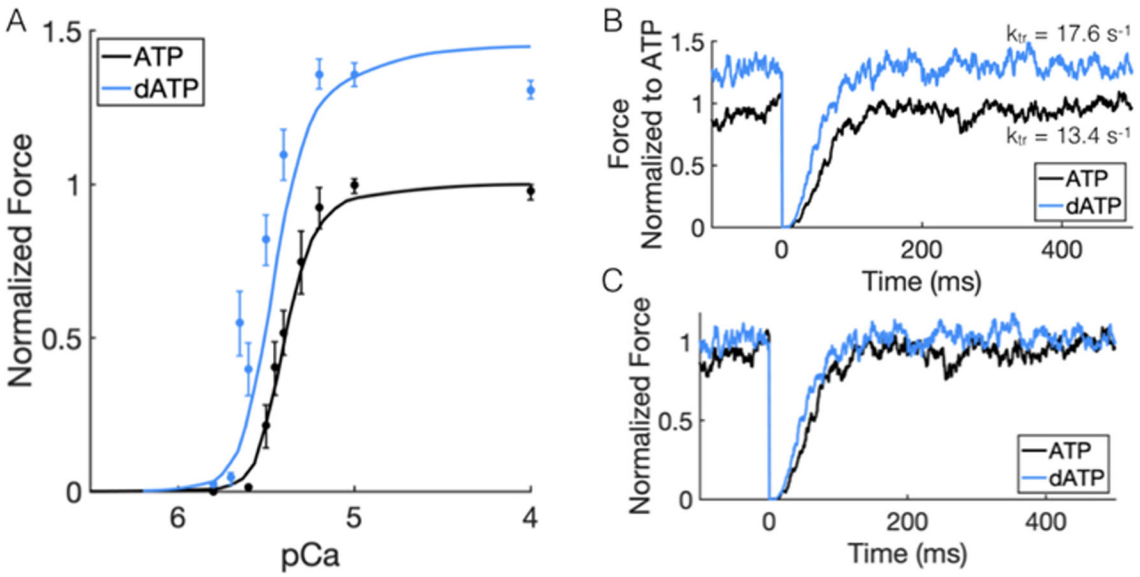

Figure 3:

A. Optimized ATP and dATP steady state curves compared to experimental data from Regnier et al. Experimental data are dots with error bars, and solid lines are simulations (black = ATP, cyan = dATP). B. Slack restretch simulations used to calculate k_{tr} for different parameter sets at pCa = 4.0 (black = ATP, cyan = dATP). Absolute forces were normalized to the maximum ATP force to demonstrate differences in steady state force production. C. absolute forces from (B) were normalized to maximum force of each simulation, to demonstrate differences in tension redevelopment kinetics.

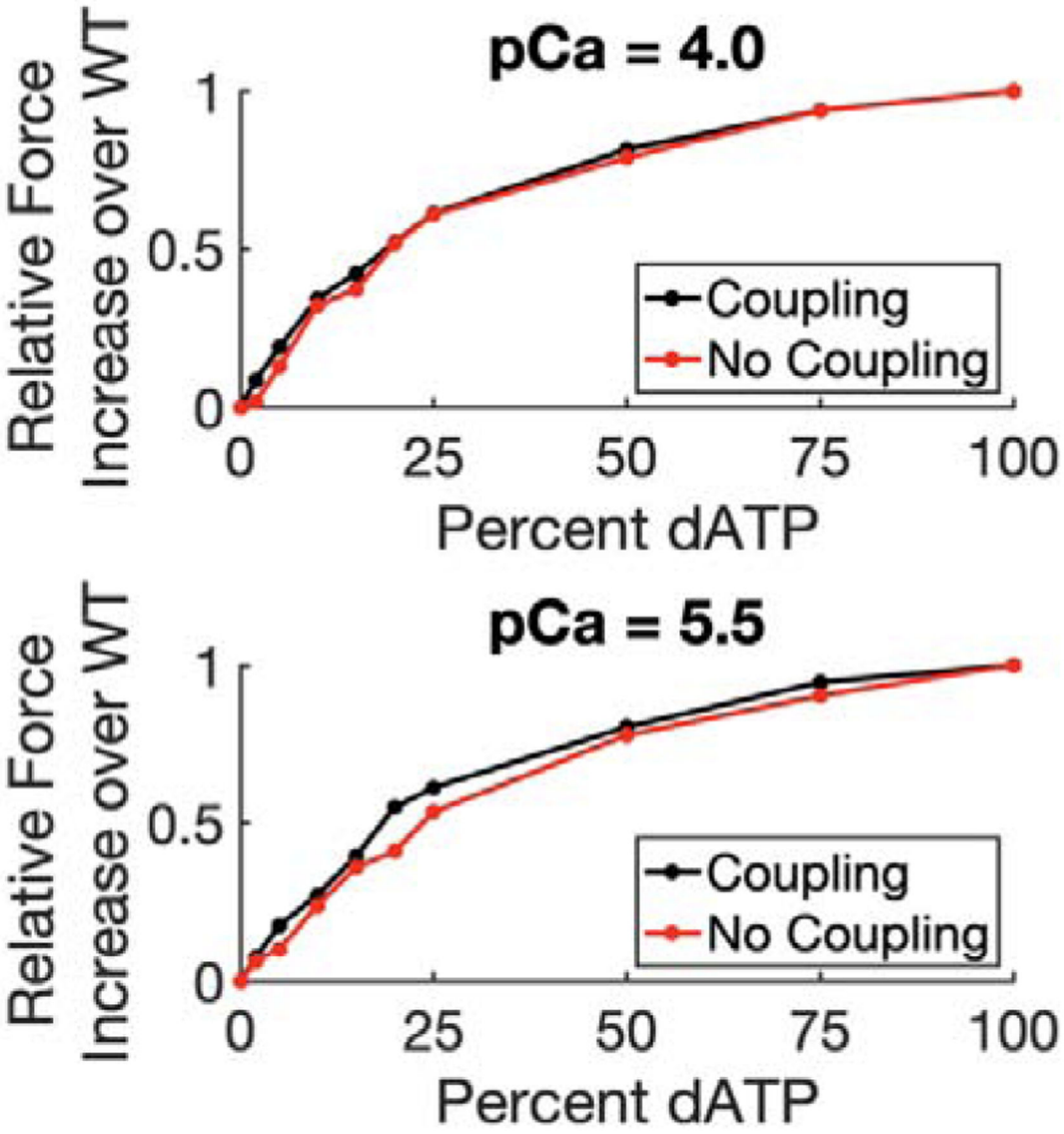

Figure 4:

Steady state force at pCa 4.0 and pCa 5.5 as a function of dATP/ATP ratio (all ATP case displayed as 0% dATP). black: RU-RU Coupling enabled, red: RU-RU coupling disabled (all cooperative coefficients = 1).

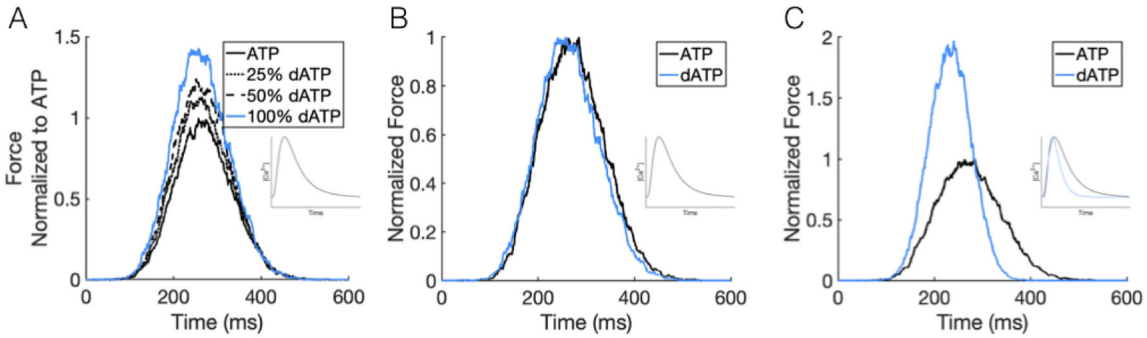

Figure 5:

Twitch simulations with experimental calcium transient inputs. A. Force (normalized to maximum ATP case force) as a function of time. The input calcium transient is displayed in the inset, and is digitized from [2]. Solid black line: ATP only. dotted line: 25% dATP. dashed line: 50% dATP. solid cyan: 100% dATP. B. Twitch results for the ATP and dATP curves from (A), normalized to the maximum force for each data set. C. Black line: ATP parameter set twitch with WT calcium transient from Korte et al. Cyan line: 100% dATP twitch with dATP treatment calcium transient from Korte et al, as indicated by the blue line in the inset.

Table 1:

Optimized parameters for ATP and dATP SS curve fitting. In the dATP case, the k_f^+ value is determined from BD, and k_p^+ and k_g^+ were optimized to fit dATP steady state and k_{tr} experimental data.

	$k_{Ca}^+\left(\mu M^{-1}ms^{-1}\right)$	$k_{Ca}^-\left(ms^{-1}\right)$	$k_B^+\left(ms^{-1}\right)$	$k_B^-\left(ms^{-1}\right)$	$k_f^+\left(ms^{-1}\right)$	$k_p^+\left(ms^{-1}\right)$	$k_g^+\left(ms^{-1}\right)$	γ_B	γ_M	μ_M	k_{tr} (s^{-1})
ATP	0.09	0.57	13	0.1	0.0025	0.05	0.135	45	21	2	13.4
dATP					0.00567	0.08	0.23				17.6